Nanoscale

PAPER

View Article Online
View Journal

Cite this: DOI: 10.1039/c6nr03916b

Multi-modal Mn–Zn ferrite nanocrystals for magnetically-induced cancer targeted hyperthermia: a comparison of passive and active targeting effects†

Jun Xie,[a,b] Caiyun Yan,[c] Yu Yan,[d] Ling Chen,[a] Lina Song,[a] Fengchao Zang,[e] Yanli An,[e] Gaojun Teng,[e] Ning Gu*[a] and Yu Zhang*[a]

The high performance and increased tumor-targeting accumulation of magnetic nanocrystals (MNCs) are the most important considerations in cancer targeted magnetic hyperthermia (TMH). To achieve these goals, our study was firstly done using well-established fluorescence/magnetic Mn–Zn ferrite MNCs (core size: 14 nm) as multi-modal imaging contrast agents and highly-efficient "heat generators", which were coated with a biocompatible PEG-phospholipid (DSPE-PEG2000) and further modified by a cyclic tri-peptide of arginine-glycine-aspartic acid (RGD). By using a mouse model bearing breast carcinoma (4T1), we then systematically compared PEGylated MNCs (MNCs@PEG)- and RGD-PEGylated MNCs (MNCs@RGD)-mediated tumor targeting abilities by intravenous administration. The MNCs@PEG-based passive targeting could successfully accumulate at the tumor due to the enhanced permeability and retention (EPR) effects, but the non-targeted localization might make the MNCs@PEG "leaking" from larger pores of tumor fenestrated vascular networks. Our designed MNCs@RGD, simultaneously functionalized with PEG and RGD ligands, might promote a synergistic effect including efficient tumor vasculature active targeting and EPR-mediated passive targeting, improving total MNC concentration and retention time in tumor tissues. By combining fluorescence/magnetic resonance (MR)/thermal multi-modal imaging-guided diagnostics and continuous TMH treatment under an alternating current magnetic field (ACMF, 2.58 kA m^{-1}, 390 kHz), the tumor surface could be heated to approximately 43–44 °C based on the MNC-mediated repeated injections. Sufficient temperature elevation induced the apoptosis of tumor cells, and inhibited the tumor angiogenesis. Compared with MNCs@PEG, the active MNCs@RGD-based tumor targeting MR image was significantly more efficient due to both the higher and long-lasting tumor accumulation, but its antitumor efficacy was not obviously improved in the TMH treatments. To achieve a singularly promising tumor TMH therapy, a greatly increased MNC content in tumor was needed. This insight indicated that not only the tumor vasculature targeting, but also the active tumor cells targeting of MNCs should receive considerable attention in future clinical TMH therapy application.

Received 14th May 2016,
Accepted 4th July 2016

DOI: 10.1039/c6nr03916b

www.rsc.org/nanoscale

Introduction

Thermal energy is emerging as an important means of stimuli-responsive functions for cancer therapy in recent years, such as conventional radio frequency-, microwave- and laser wavelength-induced thermotherapy, or promising magnetothermal and photothermal therapy.[1–8] In particular, magnetic nanoparticle (MNP)-mediated targeted magnetic hyperthermia (TMH) *in vivo* is based on the heat generated by the MNPs exposed to an alternating current magnetic field (ACMF), which provides a minimal damnification to deliver a therapeutic dose of heat specifically to cancerous regions.[4–8] The basic steps taken for the TMH involve intravenous delivery of the designed MNPs into tumors, and heating of the MNPs by

[a]*State Key Laboratory of Bioelectronics, Jiangsu Key Laboratory for Biomaterials and Devices, School of Biological Science and Medical Engineering & Collaborative Innovation Center of Suzhou Nano Science and Technology, Southeast University, Nanjing 210096, P. R. China. E-mail: zhangyu@seu.edu.cn; Fax: +86 25 8327 2460; Tel: +86 25 83272496*
[b]*School of Life Science, Jiangsu Normal University, Xuzhou 221116, P. R. China*
[c]*Department of Pharmaceutics, China Pharmaceutical University, Nanjing 210009, P. R. China*
[d]*State Key Laboratory of Coordination Chemistry, Nanjing National Laboratory of Microstructures, Nanjing University, Nanjing 210093, P. R. China*
[e]*Jiangsu Key Laboratory of Molecular and Functional Imaging, Medical School, Southeast University, Nanjing 210009, P. R. China*

†Electronic supplementary information (ESI) available. See DOI: 10.1039/c6nr03916b

using ACMF to achieve the desired therapeutic temperatures. In general, tumor cells are considered more susceptible to heat induction than normal cells due to their higher rates of metabolism. They show the signs of cell apoptosis when the tumor is heated in the range of 41 to 45 °C (milder temperatures), and cell necrosis or coagulation when heated over 50 °C (thermal ablation temperature).[7–10] In contrast to conventional thermotherapy, TMH is superior and predominant due to the following reasons: (1) it can focus on the exact location of both transplantable and *in situ* carcinoma *in vivo*, and provides a non-invasive way to efficiently raise the tumor temperatures to therapeutic levels; (2) the MNPs working as "thermal seeds" in the tumor can be visualized using magnetic resonance imaging (MRI), where the diagnostics and therapy are integrated into a single platform.[5,11] To achieve an efficient widespread clinical use of TMH, several key factors need to be considered.

Firstly, the high magnetic-induced heating potential of MNPs is an important parameter for TMH application, since it has a distinct impact on the dosages that have to be applied to the tumor in order to achieve efficient treatment.[5,11] Generally, the heating potential is determined by the size, shape, composition and microstructure of MNPs.[6,11] Over the past decade, magnetic Fe_3O_4 nanoparticles depending on a relatively high specific absorption rate (SAR) upon exposure to ACMF, had served as the conventional material in promising cancer thermotherapy.[5,11–14] In an attempt to develop new ferrite nanoparticles with higher thermal energy transfer capability, the metal dopant substitution strategy had been pursued in recent studies.[11,15–17] For instance, it was proved that this strategy for enhancing the SAR value (432 W g^{-1}) of doped $(Zn_{0.4}Mn_{0.6})Fe_2O_4$ nanoparticles was very important for achieving high and tunable magnetism. The high SAR could bring better efficacy with lower dosage levels, leading to a fourfold enhancement in hyperthermic effects *in vitro* compared to the conventional feridex measured under an ACMF (500 kHz, 37 kA m^{-1}).[5,15] So the outstanding magnetic performance makes the doped MNPs promising as excellent heating agents for TMH application *in vivo*.

Secondly, the MNP-mediated tumor-targeting efficiency also plays a vital role in practical TMH *in vivo*.[6] The MNPs without surface modification are rapidly cleared from blood circulation when passing through the biological defense system and vascular barriers. The local accumulation of these MNPs in the tumor merely relies on the distinct physiology and anatomy of tumor tissue (*e.g.*, permeable tumor vasculature).[6,18,19] The tumor endothelial gaps and improperly aligned vascular endothelium result in the "leaky" characteristic of blood vessels, enabling the extravasation of uncoated MNPs into the tumor interstitium *in vivo*. This phenomenon is called the "enhanced permeability and retention" (EPR) effect, which is an important basis for the passive targeting.[18,19] It is worth mentioning that the passive targeting of drug-loaded nanocarriers may be considered as an effective anti-cancer drug delivery system for cancer chemotherapy. It can result in increased drug concentrations of several-fold in solid tumors relative to those obtained with free drugs, based on their increased tumor specificity.[19,20] To improve the biodistribution and local concentration of MNPs at target sites by passive targeting, introduction of surface modification with some biocompatible polymers, such as polyethylene glycol (PEG), provides a stabilizing layer that prevents MNP agglomeration and enhances colloidal stability.[17,21,22] It was proved that the PEGylated MNPs could effectively reduce recognition by a reticuloendothelial system (RES) in a physiological environment, thus improving circulating properties and promoting selective accumulation in the tumor through the EPR effect.[17,21–24] The MNP-mediated passive targeting can successfully accumulate in tumors, but it also concurrently accumulates in some other tissues, most notably the liver and spleen. It makes for restricted use for the tumor TMH purpose, since the sufficient accumulation of MNPs in tumor tissues is an important consideration in TMH treatment.

As opposed to passive targeting, the MNP-mediated active targeting can be performed by the incorporation of functional groups and affinity ligands to MNP surface coating.[25] The targeting ligands are usually chosen to bind to the receptors overexpressed by tumor cells or vasculature, but not expressed by normal cells, may act as "homing devices", improving the selective delivery of MNPs to specific tumor tissues.[26,27] In active targeting, the MNPs as a "binding-site carrier" can be deposited in the tumor region after intravenous administration, which is rather challenging in the TMH. Among various ligands currently developed allowing the "active targeting" effects on tumors, the cyclic tripeptide arginine-glycine-aspartic acid (RGD) has been shown to bind preferentially to integrin $\alpha_v\beta_3$ as a specific marker of tumor angiogenesis that is overexpressed in activated and proliferating endothelial cells.[26–29] Angiogenesis as the formation of new capillaries from the preexisting vessels is essential for the development of malignant tumors. Clinical studies show that the inhibition of integrin $\alpha_v\beta_3$ activity by cyclic RGD peptide targeting with drugs can induce endothelial apoptosis, inhibit angiogenesis, and increase endothelial monolayer permeability.[30–33] Similar to chemotherapy, designing a RGD-based MNP delivery associated with preferential tumor vascular-focused TMH has the advantage of not only targeting tumor vasculature, but also simultaneously causing heat-induced tumor tissue and vascular endothelial damage, which may provide an opportunity for use as a promising and novel cancer therapy.

Given the fact that hardly any systematic comparisons were available addressing the potential TMH efficiency based on the MNP active and passive tumor targeting, we here experimentally visualized and quantified the tumor accumulation of PEG and RGD-based fluorescence/magnetic Mn–Zn ferrite nanocrystals with high performance respectively, confirmed their biodistribution and intracellular uptake, and compared their magnetically-induced heating effects exposed to an ACMF. The major advantage in our designed magnetic nanocrystals (MNCs) was their specific magnetic core–lipid shell structure. It could provide here not only inner cores with excellent magnetically-induced heat induction, but also an external

PEGylated lipid layer with remarkable biocompatibility and prolonged blood circulation properties *in vivo*. The additional advantage here we had was effective active and passive targeting-mediated tumor hyperthermia, combined with fluorescence/magnetic resonance (MR)-guided tumor imaging, which provided an important target for simultaneous tumor diagnosis and therapy. The extraordinary strategy of PEGylated MNCs (MNCs@PEG)- and RGD-PEGylated MNCs (MNCs@RGD)-mediated tumor TMH attained in our study could be attributed to a combination of five key factors listed as follows: (1) high performance MNC synthesis and optimal surface modification, (2) using an ACMF with moderate frequency and field for effective heating effects, and making sure the side effects for normal tissues are minimized, (3) adequate MNC intravenous injection dose with no obvious clinical toxicity, and effective passive or active accumulation in the tumors, (4) repetitious MNC-administered injections every other day, and sufficient hyperthermia duration (no less than 30 min) every day, (5) hyperthermia-induced cell apoptosis and anti-angiogenesis in tumor tissue observed at the cellular and molecular levels.

Results and discussion

Characterization of Mn–Zn ferrite MNCs

The oleic acid (OA)-coated Mn–Zn ferrite MNCs were synthesized *via* high-temperature decomposition of metal acetylacetonate (acac) in the presence of a surfactant in our past work.[16,17] These MNCs revealed the perfect crystalline structure and highly efficient Mn/Zn dopant substitution, which was advantageous for their further biomedical application.[16] The bare MNCs were further coated with PEG and RGD molecules according to previous work,[17,28] which is shown schematically in Fig. 1(a). Both the as-synthesized Mn–Zn ferrite MNCs@PEG and MNCs@RGD had an ideal magnetic core (14 nm)–lipid shell (3.5 nm) structure. The white lipid layer surrounding the individual magnetic core was clearly observed by negatively staining with phosphotungstic acid, indicating their successful surface modification, which was determined by TEM [Fig. 1(b)]. A comparison of hydrodynamic diameters of MNCs@PEG and MNCs@RGD is shown in Fig. 1(c), in which MNCs@PEG revealed a considerably smaller hydrodynamic diameter (42.3 nm) than MNCs@RGD (54.6 nm). Note that both of these MNCs did not exhibit significant changes in hydrodynamic diameters after being kept in aqueous solution for 4 weeks [Fig. S1 in the ESI†], demonstrating their high colloidal stability. The measured zeta potentials of MNCs@PEG and MNCs@RGD were −43.9 and −16.7 mV respectively, indicating the successful conjugation of a RGD molecule to the PEG terminal of MNCs@PEG.

It was demonstrated that the magnetism of MNCs could be greatly influenced by substitution with a magnetically susceptible Mn or Zn element.[15] As is shown in Fig. 1(d), the hysteresis loop at room-temperature (300 K) displayed extraordinarily high saturation magnetization values (M_s) of 112 and 115 emu g^{-1} Fe for MNCs@PEG and MNCs@RGD, respectively. The hysteresis loop showed essentially no coercivity (H_c) for both of the MNCs, exhibiting their remarkable superparamagnetism. Generally, the high M_s values of the MNCs tended to obtain distinct magnetically-induced heat generation under an ACMF and achieve the enhanced MRI contrast effect.[5,11] Our synthesized MNCs have a high thermal energy transfer capability when exposed to an ACMF (2.58 kA m^{-1}, 390 kHz). From Fig. 1(e), the MNCs@PEG and MNCs@RGD possessing the high SAR values of 498 and 532 W g^{-1} Fe, induced temperature elevation by approximately 36 °C and 39 °C in aqueous solution at a concentration of 2 mg of Fe per ml for 15 min exposure under the ACMF, respectively. In MRI, both MNCs@PEG and MNCs@RGD displayed a clear concentration-dependent T_2 signal reduction effect, which was shown by the MR contrast changing from light gray to black as the concentration of MNCs increased. The corresponding relaxivity coefficient (r_2) values of 485 and 501 mM^{-1} s^{-1} were calculated by the plot of R_2 *versus* the molarity of Fe [Fig. 1(f)]. Here the MNCs@RGD typically showed that the SAR value and MR contrast effect were appreciably superior to that of MNCs@PEG, which might lie in the partial aggregation formation of MNCs due to the cross-linking effect of surface polypeptide.

Cellular binding and uptake of Mn–Zn ferrite MNCs *in vitro*

To assess the ability of MNCs to escape RES such as macrophage uptake, and to specifically bind target tissue, we firstly conducted *in vitro* cellular uptake experiments as a prelude to *in vivo* studies, by using RAW 264.7 macrophages, mice breast cancerous (4T1) and human umbilical vein endothelial cells (HUVECs) incubated with MNCs@PEG, MNCs@RGD and dimercaptosuccinic acid (DMSA)-modified MNCs (MNCs@DMSA) for comparison respectively. The cellular uptake of MNCs was assessed using Prussian blue staining, which is shown in Fig. 2(a–c). For the above-mentioned three types of cells, after incubation with MNCs@PEG and MNCs@RGD for 12 h and washing with PBS, no distinct blue color could be detected, demonstrating that both the MNCs could drastically minimize the recognition and phagocytosis of macrophages and other cells predicting that our designed MNCs can escape RES uptake *in vivo*. Most of the RAW 264.7 cells incubated with MNCs@DMSA, as the contrast group, were stained blue color, indicating that the mass of MNCs@DMSA could be readily phagocytized to macrophages.

Generally, the cell adhesion molecule $\alpha_v\beta_3$ integrin is a specific marker of angiogenesis, which is overexpressed in activated and proliferating endothelial cells, such as HUVEC cell lines.[28] Here our results showed that MNCs@RGD specifically bound with high affinity to $\alpha_v\beta_3$ integrin of HUVECs, and subsequently accumulated in the cytoplasm after the 12 h incubation (blue color marking) [Fig. 2(b3) and Fig. S2†], whereas, there was no significant cellular uptake for MNCs@RGD in the presence of free RGD, added as a competitive inhibitor, indicating that the accumulation of the MNCs@RGD was specifically mediated by their $\alpha_v\beta_3$ integrin binding, but not the nonspecific binding [Fig. 2(b4)]. It was worth mentioning that

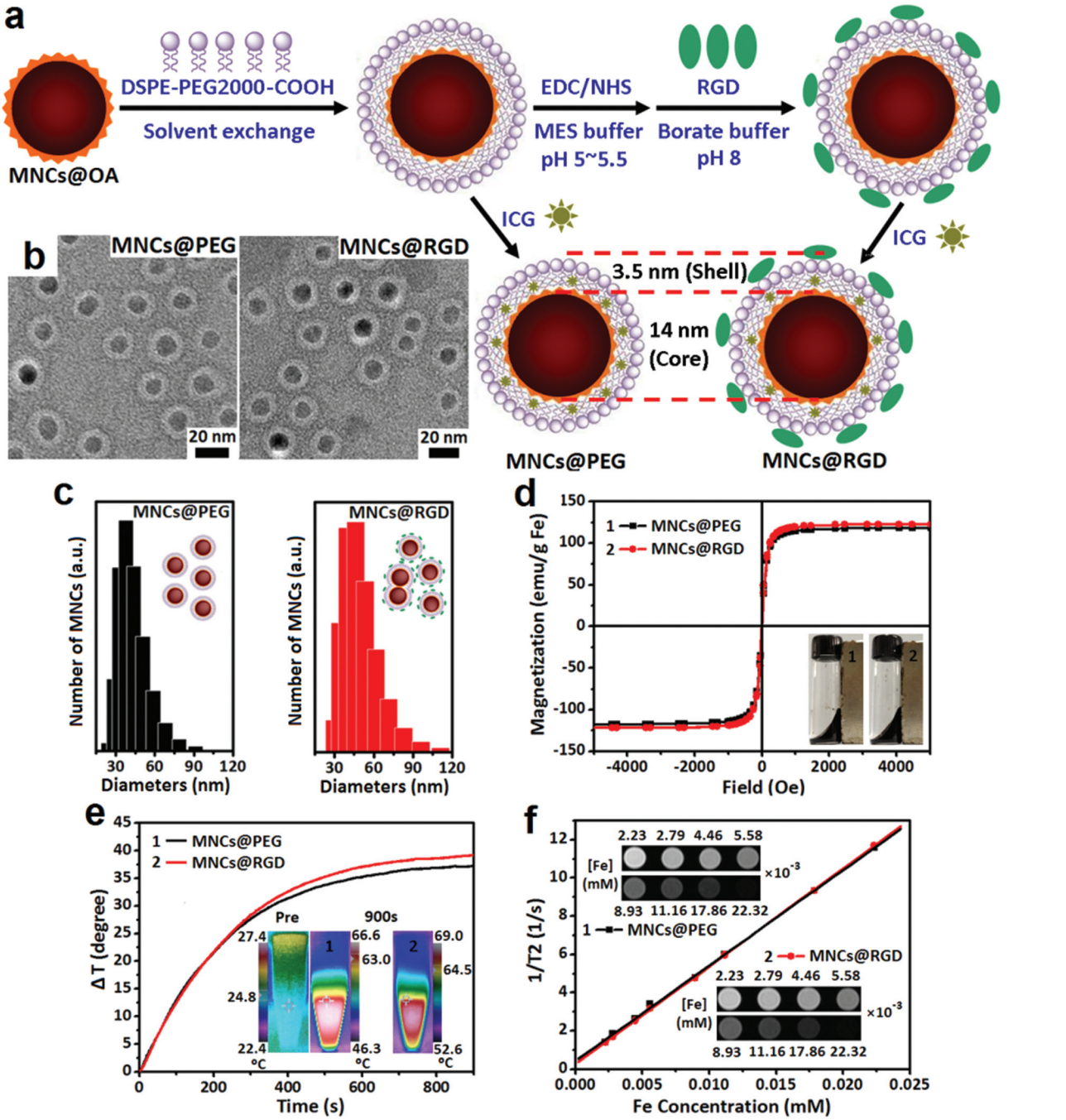

Fig. 1 (a) A schematic diagram of ICG-loaded Mn–Zn ferrite MNCs@PEG and further MNCs@RGD synthesis. (b) TEM images of MNCs with a core–shell structure negatively stained with 2% phosphotungstic acid to give a white layer surrounding the magnetic cores, indicating the coating lipid layer. (c) DLS measurement of MNCs in water. (d) Hysteresis loops and digital images of MNCs. (e) Time–temperature curves of MNCs in the aqueous phase (2 mg Feper ml) and the corresponding *in vitro* thermal images under ACMF (390 kHz, 2.58 kA m^{-1}). (f) T_2-Weighted MR images and dependency of relaxation time of MNCs upon iron concentration measured by a 1.5 T MR scanner.

the amount of bound MNCs@RGD was believed to depend on the receptor expression level and ligand–receptor binding affinity. In line with this finding, the MNCs@RGD uptake in 4T1 cells with less $\alpha_v\beta_3$ integrin receptors at the same conditions was less prominent [Fig. 2(c3)].

In addition, a key consideration for the *in vivo* use of MNCs was to assess their potential biocompatibility. In this regard, the *in vitro* cytotoxicity of MNCs@PEG and MNCs@RGD with various incubation concentrations (0–160 μg of Fe per ml) for 48 h was evaluated with a MTT (3-(4,5-dimethylthiazol-2-yl)-2,5-diphenyltetrazolium bromide) assay using RAW 264.7, 4T1 and HUVECs cell lines (Fig. S3†). Comparatively, no appreciable toxicity was observed up to the highest concentration in the MNCs@PEG treatment groups. The MNCs@RGD also did

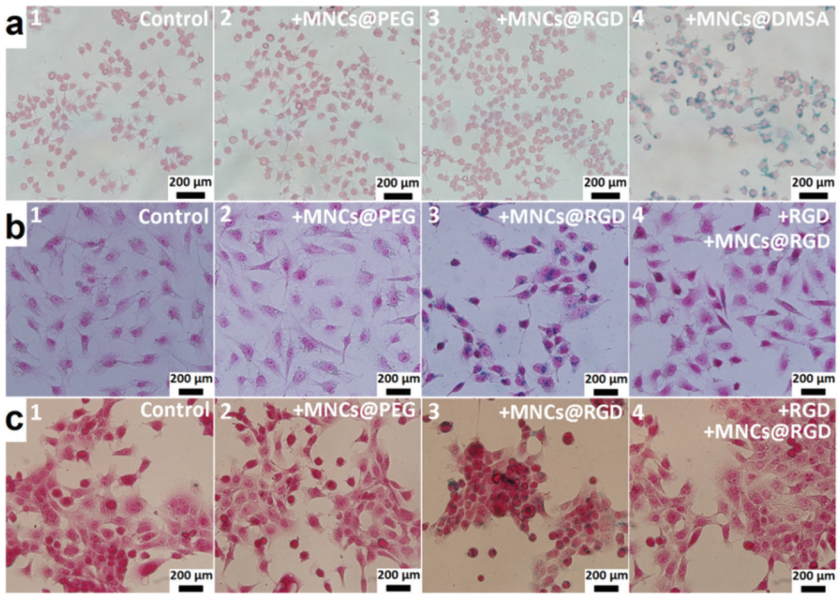

Fig. 2 Cellular uptake testing *in vitro* with Prussian blue staining images of (a) RAW 264.7 macrophages, (b) HUVECs and (c) 4T1 cells after 12 h treatment with Mn–Zn ferrite MNCs@PEG, MNCs@RGD, and MNCs@DMSA at a concentration of 60 μg Fe per ml. Control group here indicated the cells not incubated with MNCs.

not cause a significant decrease in viability for RAW 264.7 and 4T1 cell lines at the same dose, but exhibited lower cytotoxicity (70–75% levels of cell viability) for HUVEC cell lines at the corresponding Fe concentration up to 140–160 μg ml^{-1}. This should be attributed to the intracellular localization of MNCs@RGD with the specific binding affinity mentioned above.

Biodistribution and intracellular uptake of Mn–Zn ferrite MNCs *in vivo*

On the basis of the successful *in vitro* experiments, we here established mouse models of 4T1 breast tumor and performed *in vivo* fluorescence imaging based on incorporating indocyanine green (ICG) as a tricarbocyanine dye in MNCs@PEG and MNCs@RGD delivery systems, to real-time monitor the localization and biodistribution of MNCs (30 mg Fe per kg body weight). From the whole body fluorescence signals [Fig. 3(a)], we distinctly observed the MNC tracking, accumulation, and clearance. For both MNCs@PEG and MNCs@RGD, intense fluorescence signals were observed throughout the mouse body by blood circulation over 0–2 h after the injection through the tail vein. Nevertheless, the fluorescence signals gradually enhanced and mainly located around the tumor regions after 4 h post-injection, and reached a maximum until a duration of 24 h. The results indicated that the MNCs coated with PEG layers apparently circulated longer in the bloodstream, and finally passively or actively accumulated into the tumor regions. 24 h post-injection of MNCs@PEG and MNCs@RGD, it was also important to note the differences in fluorescence signals of tumors. Fluorescence intensity of the tumors and adjacent muscles was semi-quantitatively analyzed

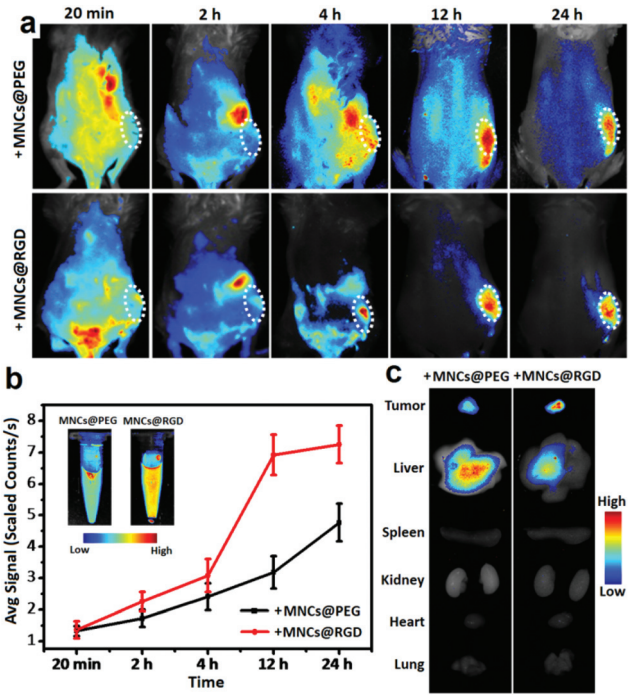

Fig. 3 (a) Fluorescence images of mice bearing breast cell carcinoma (4T1) acquired after the intravenous injection of Mn–Zn ferrite MNCs@PEG and MNCs@RGD (30 mg Fe per kg body weight) at different times. (b) Average fluorescence signal of TBR in MNCs@PEG-targeted and MNCs@RGD-targeted groups at different post-injection times, and the data are shown as mean ± SD (n = 3). The inset shows the *in vitro* fluorescence imaging of MNCs. (c) Fluorescence images of main organs (tumor, liver, spleen, kidney, heart and lung) of mice 24 h post injection of MNCs@PEG and MNCs@RGD.

to determine the targeting ability of the MNCs at different time intervals [Fig. 3(b)]. The average target-to-background ratio (TBR) signal values were 1.32, 1.71, 2.40, 3.18 and 4.77 at 20 min, 2 h, 4 h, 12 h and 24 h in MNCs@PEG-targeted groups, and were 1.34, 2.25, 3.08, 6.93 and 7.26 at the same intervals in MNCs@RGD-targeted groups. These differences were statistically significant ($P < 0.05$).

To give a more clear comparison of the passive and active targeting effects of MNCs *in vivo*, major organs (heart, liver, spleen, lung and kidney) and tumors were excised 24 h post-injection. As shown in Fig. 3(c), the fluorescent signal at liver tissue strongly presented in the MNCs@PEG intravenous administration group, but became weaker in the group after the injection of MNCs@RGD. In addition, the fluorescence intensity at the tumor tissue was more enhanced following the injection of MNCs@RGD than that of MNCs@PEG. These results together reflected the EPR-mediated *in vivo* passive targeting of MNCs@PEG could escape from RES entrapment, achieving efficient accumulation in tumor sites. But the non-targeting ability of MNCs@PEG might make them "leak" from the larger pores of fenestrated vascular networks in tumor, leading to further uptake of MNCs in the liver and spleen. For MNCs@RGD, the enhanced tumor binding affinity and reduced MNC uptake in liver and spleen organs were significantly promoted by the simultaneous assistance of PEG chains and RGD peptides. Such a pronounced fate was also demonstrated by stained histological sections (Fig. S4†).

In contrast, when intravenously injected with free ICG molecules, no noticeable fluorescence signal was observed in the tumor sites 24 h post-injection (Fig. S5†). The reason lay in the relatively short circulation time of the free ICG *in vivo*. The free ICG molecules were rapidly taken up by the liver, and passed through the bile and came into the alimentary canal for excretion, resulting in their fluorescence quenching in physiological environments. Here it provided direct evidence that the encapsulation of ICG molecules inside a lipid layer of MNCs, could avoid suffering from metabolism, leading to stronger fluorescent signals than free ICG molecules.

To accurately compare the tumor histologic localization of passive- or active-targeted MNCs, the nuclear fast red, CD31 immunohistochemical and Prussian blue stained tumor tissue slices were respectively prepared 24 h post-injection of MNCs@PEG and MNCs@RGD, which were analyzed *via* optical microscopy. As is shown in Fig. 4(a–c), the stained tumor tissue showed heterogeneous vascularization with large and intensively branched vascular networks (brown stained). In MNC treatment groups, it indicated that both passive-targeted MNCs@PEG and active-targeted MNCs@RGD could

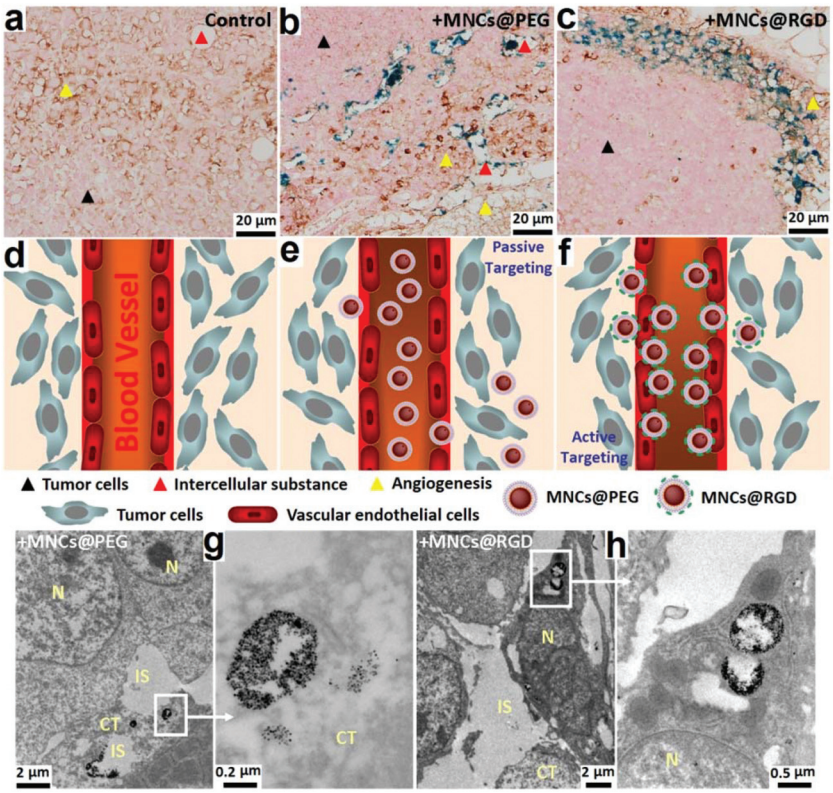

Fig. 4 (a–c) The nuclear fast red, CD31 immunohistochemical and Prussian blue stained images of tumor tissue slices of control mice and the mice after the intravenous administration of passive-targeted Mn–Zn ferrite MNCs@PEG and active-targeted MNCs@RGD. (d–f) The corresponding schematic diagram involved in MNC-mediated passive and active tumor targeting. (g, h) Biological TEM images of tumor tissue slices and the partial magnification showing the subcellular distribution of MNCs@PEG and MNCs@RGD. Remark: N: nucleus, IS: intercellular substance, and CT: connective tissue.

accumulate in tumor tissue based on the existence of many blue stained aggregates [Fig. 4(b and c) and Fig. S6†]. For passive-targeted MNCs@PEG, no significant cellular uptake and binding effect on tumor cells or vascular endothelial cells was detected, and the MNCs@PEG were mainly dispersed in the gaps between tumor cells, providingevidence of the MNCs@PEG effect on phagocytosis resistance during blood circulation *in vivo*. But for active-targeted MNCs@RGD, except for the intercellular localization, they were proved to maximize target recognition and to bind tumor vascular endothelial cells with $\alpha_v\beta_3$ integrin, leading to significant accumulation at the tumor vasculature. The corresponding schematic diagrams involving passive accumulation *versus* active targeting effects of MNCs@PEG and MNCs@RGD on tumor cells and vasculature are shown in Fig. 4(d–f).

In order to further clearly investigate the intracellular localization of MNCs, a comparison was made with biological TEM images of correlative tumor tissue slices, as exemplified in Fig. 4(g and h). To elaborate, the MNCs@PEG could be observed in the intercellular substance (IS) or the tumor connective tissue (CT). For MNCs@RGD, a few small aggregates consisting of single uniformly distributed MNCs were incorporated preferably into the cytoplasm and endosomes of tumor vasculature cells. It was speculated that the conjugation of tumor vascular endothelial cells with high integrin $\alpha_v\beta_3$ expression and cyclic RGD peptide on the MNC surface might promote receptor-mediated endocytosis, which was an important pathway for the cellular internalization of MNCs@RGD. The TEM investigation revealed discrepant sub-cellular distribution of passive- and active-targeted MNCs in tumor tissue, and was in accordance with the above immunohistochemistry analysis.

Accumulation and retention duration of Mn–Zn ferrite MNCs in tumor tissue detected by real-time T_2*-weighted MR imaging

To give more evidence of the *in vivo* targeting effects, accumulation and retention duration of MNCs in tumor sites, the real-time T_2*-weighted MR images at the tumor region over time (0–96 h) after the MNC injection (30 μg Fe per g body weight) are shown in Fig. 5(a). There were obvious dark dots in a fraction of the tumor 4 h post-injection of both MNCs@PEG and MNCs@RGD. With time, the whole tumor area was becoming much darker than that before administration until 24–48 h, suggesting a large amount of MNCs was accumulating in the tumor area. In the course of time (usually 48–96 h), the passively-targeted MNCs@PEG-induced MR signal darkening in tumor regions gradually disappeared, meaning the "leaking" characteristic of MNCs@PEG might induce their excretion, and clearance by correlative organs *in vivo*. In comparison, after active-targeted MNCs@RGD injection, a spot of darker dots still existed in tumor partial regions as long as 96 h, which provided strong evidence that the MNCs@RGD possessed the imaging ability of prolonged tumor targeting

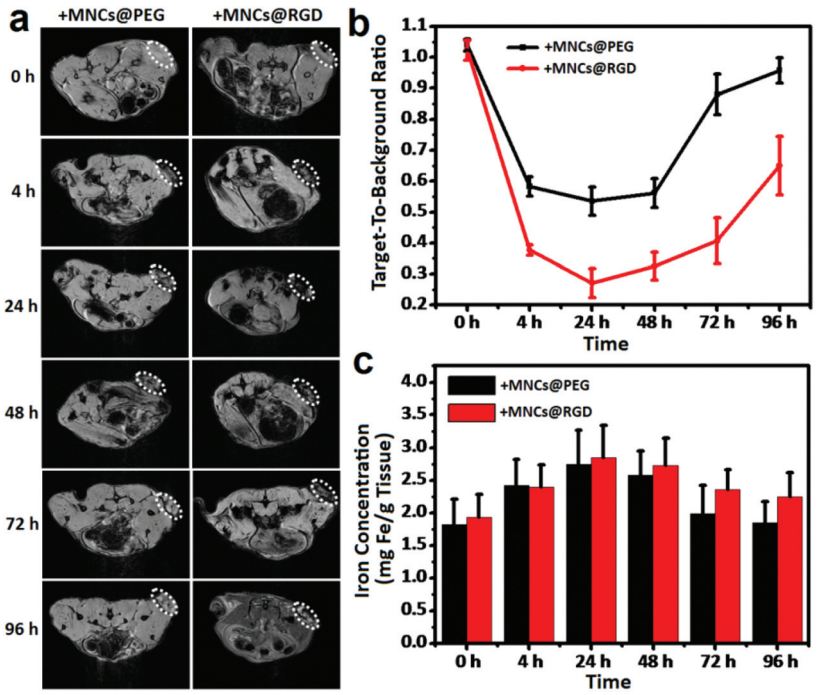

Fig. 5 (a) T_2*-Weighted MR images of mice tumor real-time targeting characteristics acquired before and after intravenous injection of Mn–Zn ferrite MNCs@PEG and MNCs@RGD (30 μg Fe per g body weight) at different times (0–96 h) using a 7 T MR scanner. After administration of MNCs, the MR signal of the tumor site is significantly attenuated. (b) Average signal of MRI-based TBR in the MNCs@PEG-targeted and MNCs@RGD-targeted groups at different post-injection times (0–96 h). (c) The corresponding Fe amounts in mice tumor tissue after treatment with MNCs@PEG and MNCs@RGD at different times (0–96 h). The data of (b, c) are shown as mean ± SD (n = 3).

in vivo. The time-dependent darkening of the MR images of tumor tissue after the administration of the MNCs was also confirmed quantitatively, based on the TBR values between the tumor and the adjacent normal muscle [Fig. 5(b)]. But surprisingly, the quantitative kinetic studies of MNC tumor uptake levels (measured Fe mass per gram of tumor) had not shown notable difference of Fe concentration in tumor tissue between MNCs@PEG and MNCs@RGD treated groups over 0–96 h [$P > 0.05$, Fig. 5(c)]. These results indicated that the T_2*-MRI was more sensitive for MNC uptake in tumor tissue, especially for the slight difference of Fe concentration in tumor tissue.

Mn–Zn ferrite MNC-mediated cancer theranostics combining MRI and ACMF

TMH has recently emerged as a promising therapeutic approach for cancer treatment due to the intravenous administration of MNCs to deliver a therapeutic dose of heat specifically to the cancerous regions under ACMF.[5–8] An essential challenge in effective TMH is the efficient accumulation of MNCs with high-performance in tumor tissues. However, it was proved that the single-injection of MNCs was difficult for achieving the necessary concentration in the tumor regions. In this regard, we described the use of MNCs@PEG and MNCs@RGD with a well-tolerated intravenous dose by repeated intravenous injections (3 times, single dose of 30 μg Fe per g body weight), and then the tumors were repeatedly heated at least for 30 min at a single hyperthermia time every day using ACMF of 2.58 kA m^{-1} at 390 kHz over 7 days. The total amount of MNCs used here was considerably larger than that used in previous MRI imaging, but no obvious signs of toxicity were observed (no weight loss or abnormal behavior) over the course of 4 weeks owing to the biocompatibility of lipid-coated MNCs.

This strategy here was designed for effective imaging and TMH therapeutics, which include MRI diagnostics with high sensitivity and heat emission treatment in succession, as shown in Fig. 6(a). In Fig. 6(b), the T_2- and T_2*-weighted MRI as a diagnosis tool indicated that the long-circulating MNCs@RGD with vascular target-affinity could effectively and lastingly concentrate in tumor tissues over the 7 days of theranostics. In contrast, the MNCs@PEG might preferentially accumulate in tumor tissue owing to the passive EPR effect for

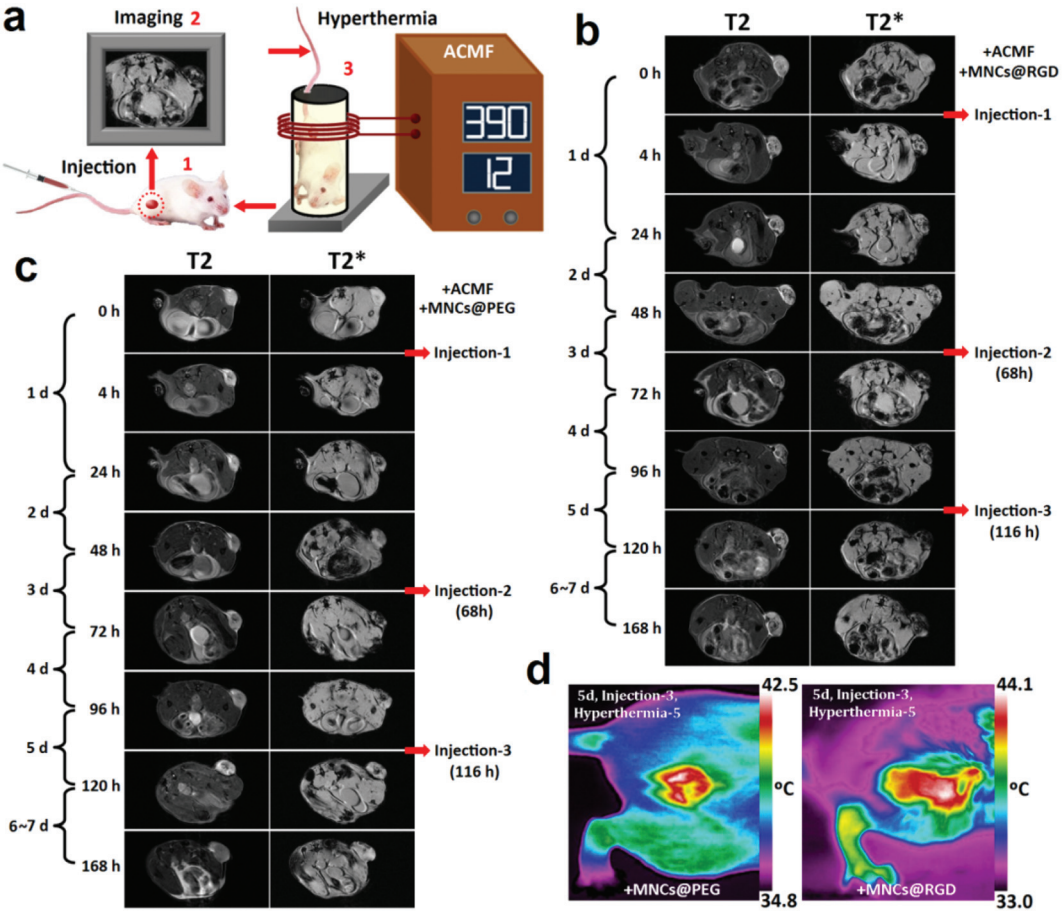

Fig. 6 (a) A schematic diagram of Mn–Zn ferrite MNCs for magnetically induced cancer theranostics combining MRI and ACMF (390 kHz, 2.58 kA m^{-1}). (b, c) T_2 and T_2*-weighted MR images of mice acquired before and after the repeated intravenous injection of MNCs (single dose: 30 μg Fe per g body weight, 3 times) and ACMF actions (7 times, once a day) at different times (0–7 days) using a 7 T MR scanner. (d) Thermal images of mice tumor after the 3rd intravenous injection and 5th magnetically-induced hyperthermia using MNCs under the ACMF.

a short time after intravenous injection. But over time, the passive targeting of MNCs@PEG was significantly more inefficient, in MRI, attributed to the leakage of MNCs@PEG from the tumor blood vessel [Fig. 6(c)]. After more reduplicative MNCs@PEG and MNCs@RGD injection and TMH, the corresponding recorded average and maximum heating temperature of the tumor surface was approximately between 39 and 44 °C (from the 1st day to the 7th day in theranostics), detected by an infrared-thermograph (Table 1). For instance, the local maximum temperature in the tumor surface achieved 42.5 and 44.1 °C respectively on the 5th day [Fig. 6(d)]. These distinct temperature elevations could absolutely lead to tumor cell apoptosis. It was also obvious that MNCs@RGD-guided active TMH was rather challenging, since it could provide a relatively higher heating power (the tumor surface maximum temperature increased by 1.6 °C) based on the prolonged accumulation of MNCs in the tumor region.

TMH-induced cell apoptosis and anti-angiogenesis in tumor tissue

Generally, mild hyperthermia in combination with long-circulating MNCs, referred to smaller temperature rise, usually up to 42–45 °C, rendering the tumor tissue susceptible to various forms of apoptosis and antiangiogenesis.[6–9] The apoptosis-inducing effects of TMH in tumor regions after the 3rd intravenous injection of MNCs on the 5th day were examined by terminal deoxynucleotidyl transferase mediated deoxyuridine triphosphate-biotin nick end-labeling (TUNEL) staining [Fig. 7(a)]. In the case of MNCs@PEG- and MNCs@RGD-mediated intravenous injections, the apoptotic cell population (stained brown, 45.57 ± 5.81% and 59.12 ± 7.63%, $P < 0.05$, respectively) of the tumor tissues exposed to an ACMF was much greater than the value of tumor cells exposed to ACMF without MNC injection (6.41 ± 4.87%), indicating that the cell apoptosis was mainly attributed to the MNC-induced thermal destruction effects. Altogether, the MNCs@RGD was shown to promote apoptotic death of cancer cells in tumor tissues to a far greater extent, as compared to MNCs@PEG, showing a distinct apoptosis signal.

Except for the apoptosis of tumor cells, the heat-induced changes of vascular damage in tumor tissues following hyperthermia has also become an important anti-tumor strategy.[36] The hyperthermia is an angiogenesis inhibitor in tumor treatment through decreasing the production of the tumor-derived vascular endothelial growth factor.[36,37] To quantitatively identify the TMH-induced anti-angiogenesis effects, we used microvessel density (MVD) defined as the mean number of microvessels, which is determined by the CD31 immunostaining for the new microvasculature of the tumor tissue [Fig. 7(b)]. The branched MVD (numbers per 400 × field, brown stained) in our study was decreased remarkably in tumors of combination TMH in the presence of MNCs@PEG and MNCs@RGD (49.53 ± 5.76 *vs.* 41.88 ± 7.25) when compared with the control tumor group acted only by ACMF exposure without MNC injection (65.73 ± 8.21). The result indicated that the passive or active TMH variously increased the inhibition of tumor associated angiogenesis *in vivo*. This anti-angiogenesis effect might be attributed to two aspects as follows. On the one hand, the extreme susceptibility to heating effects was likely to be explained by the inherent abnormalities of tumor vasculature or by the inhibition of tumor-associated angiogenesis. A threshold thermal exposure above 42 °C for a mild hyperthermia treatment would result in tumor vascular damage and reduction in tumor blood flow in the vasculature,

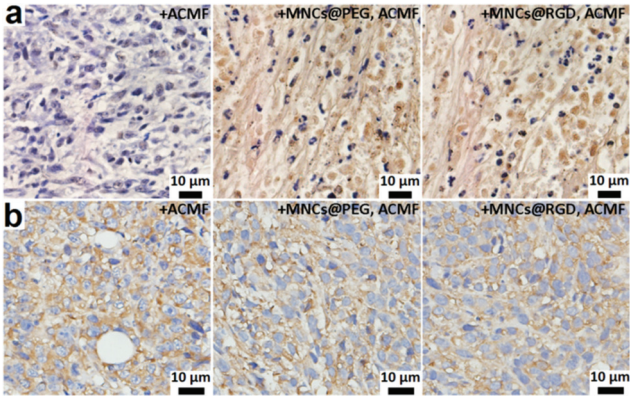

Fig. 7 (a) TUNEL staining assay and (b) immunohistochemistry of CD31 of mice tumor tissue sections after repeated intravenous injection of Mn–Zn ferrite MNCs (single dose: 30 μg Fe per g body weight, 3 times) and TMH treatments (5 times, once a day) under the ACMF actions (390 kHz, 2.58 kA m^{-1}) on the 5th theranostics day.

Table 1 Temperatures of the tumor surface after the Mn–Zn ferrite MNC-induced TMH detected by thermal images[a]

MNC-based hyperthermia (times)	Average temperature (°C)		Maximum temperature (°C)		Minimum temperature (°C)	
	G1[b]	G2[c]	G1[b]	G2[c]	G1[b]	G2[c]
1	38.0	39.3	39.4	40.1	37.2	37.8
2	37.4	38.6	38.7	39.6	37.0	37.5
3	40.8	41.5	42.3	43.2	39.2	40.6
4	40.3	41.2	41.3	42.8	39.0	40.2
5	41.3	42.8	42.5	44.1	40.5	41.7
6	41.0	42.3	41.8	43.1	40.2	41.5
7	40.3	42.0	41.2	42.8	39.7	40.8

[a] Parallel group $n = 3$. [b] Group 1: intravenous administration of MNCs@PEG. [c] Group 2: intravenous administration of MNCs@RGD.

thereby impairing oxygen and nutrient supply, affecting microcirculation in tumor tissues and inducing anti-angiogenesis effects. On the other hand, it was evident that the efficient tumor vasculature or perivascular tissue targeting effects of MNCs might produce sufficient heat induction in the tumor region, which played a fundamental role in tumor antiangiogenesis therapy. An interesting finding on tumor vasculature in previous studies is the presence of surrounding fibrous connective tissue, which support the parenchyma, carry blood supply, and also control the intratumor environment.[36,37] For MNCs@PEG, they were proved to mainly disperse in tumor IS or CT. The mediated passive TMH would indirectly lead to the retardation of tumor blood flow due to the aforementioned blood supply mechanism, which was an important pathway for antiangiogenic activity. Among the various elements of the heat-induced vascular changes, the endothelial cells may be the most important possible targets of thermal injury. So we considered that the MNCs@RGD-induced retardation of tumor microcirculation under an ACMF was caused by a combination of intravascular or perivascular events, including MNC aggregation and the corresponding heat-induction in tumor vessel endothelial cells and perivascular CT. Thus, to a large extent, the MNCs@RGD-mediated active TMH would result in enhanced endothelial apoptosis and angiogenesis inhibition *in vivo*.

In vivo antitumor efficacy

To achieve effective antitumor effects *in vivo*, we performed a therapeutic strategy using more reduplicative and long-lasting MNC injection (6 times) and hyperthermia (15 times) in 15 days (Table 2). In this strategy, the amount of intravenous-administered MNCs delivered to the tumors was enough in combination with multiple TMH periodicities to significantly inhibit the growth of tumors, compared with the control group (no MNC injection but ACMF exposure), which is shown in Fig. 8(a and b). The results indicated that the MNC-mediated TMH ultimately resulted in delay in the tumor growth within a certain period of time. To elaborate, the MNCs@PEG and MNCs@RGD had relative tumor volume ratio (RTV) growth values of only ~120 and 80% on the 15th day (P = 0.054, >0.05), which were much lower than that of ~770% for the control group (only ACMF exposure) [Fig. 8(b)].

In the MNCs@PEG group, because of the "leak" character of MNCs@PEG, on stopping the MNCs@PEG injection, no efficient MNC accumulation was detected in the interior of the tumor from the above MRI results [Fig. 6(c)]. Compared with the passive MNCs@PEG, the active MNCs@RGD-based tumor accumulation was significantly more efficient from the MRI results, but their antitumor efficacy distinction was not clear from the 13th to 15th day (P > 0.05). Indeed, the key advantage of MNCs@RGD-mediated vascular active targeting did work, which resulted in efficient binding to the tumor blood vessels, continuous accumulation and longer retention of MNCs with high concentrations in tumor tissue, whereas these advantages did not endow MNCs@RGD with more dramatically improved heat induction under ACMF action [Fig. 8(c)]. In our previous description, the RGD-grafted MNCs possessed a PEG chain and a cyclic RGD peptide, simultaneously endowing them with a passive EPR effect and an active tumor vasculature endothelium targeting effect *in vivo*. This synergistic effect would facilitate higher and long-lasting concentration of MNCs@RGD in tumor regions, which was beneficial and sensitive for the cancer MRI *in vivo* (Fig. 6). However, this advantage of MNCs@RGD-mediated MRI *in vivo* was not reflected in the following *in vivo* tumor TMH. Compared with MNCs@PEG, the MNCs@RGD-induced active TMH here only made the tumor surface temperature increase by 1–2 °C, which was not nearly enough for our desired improved TMH. To achieve singularly promising tumor TMH therapy, greatly increased MNC content in tumor tissue was further needed. This insight indicated that not only the tumor vasculature targeting, but also the active tumor cell targeting of MNCs should receive considerable attention in future clinical TMH therapy application.

In addition, it had also been observed that the tumor volume over 15 days in other control groups (only the MNC injection but with no ACMF exposure, Fig. S7†) increased obviously, indicating that the MNC administration alone would not remarkably induce tumor cell apoptosis. This result was in agreement with our above *in vitro* work, which had suggested that the MNCs had lower cytotoxic effects on 4T1 cells, based on their biocompatibility.

Table 2 The *in vivo* antitumor efficacy strategy of Mn–Zn ferrite MNCs@PEG and MNCs@RGD as passive or active-targeted agents for TMH treatments[a]

Days	MNCs intravenous injection[b] (times)	MNC-based hyperthermia[c] (times)
1	1	1
2	—	2
3	2	3
4	—	4
5	3	5
6	—	6
7	4	7
8	—	8
9	5	9
10	—	10
11	6	11
12	—	12
13	—	13
14	—	14
15	—	15

[a] Parallel group n = 5. [b] Repetitious intravenous injection of MNCs at a single dose of 30 μg Fe per g body weight every other day. [c] Sufficient hyperthermia duration (30 min) every day (with an ACMF of 2.58 kA m^{-1} at 390 kHz).

Experimental

Mn–Zn ferrite MNC synthesis

The OA-coated Mn–Zn ferrite MNCs were synthesized by a thermal decomposition method and further coated with DMSA according to our previous work.[16,17] In the MNCs@PEG synthesis, DSPE-PEG2000-COOH (1,2-distearoyl-*sn-glycero*-3-phos-

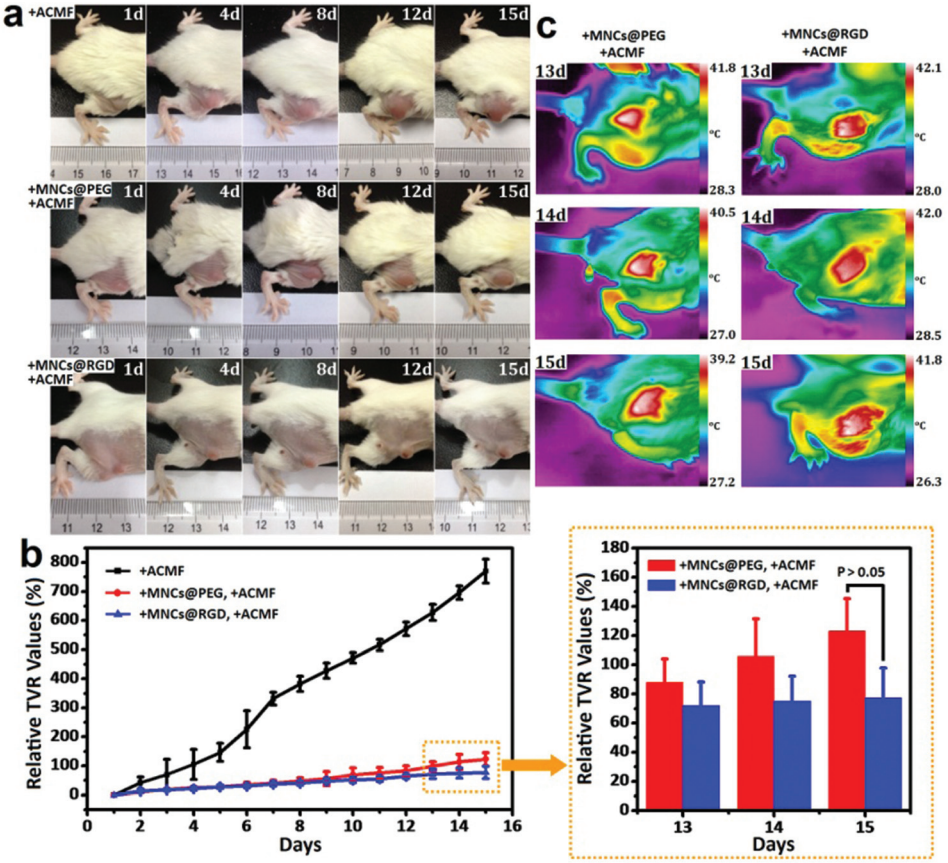

Fig. 8 (a) Photographs and (b) tumor growth behavior of mice without treatment and with treatment by repeated intravenous injection of Mn–Zn ferrite MNCs (single dose: 30 mg Fe per kg body weight, 6 times) and TMH treatments (15 times, once a day) under ACMF action (390 kHz, 2.58 kA m^{-1}) in 15 days, and the right amplified section indicates the relative TVR values of tumor growth curves after the 6th intravenous injection of MNCs and 12th TMH under an ACMF from the 13th to 15th day. The data are shown as mean ± SD (n = 5). (c) Thermal images of the tumor surface after the 6th intravenous injection of MNCs and 12th TMH under an ACMF from the 13th to 15th day.

phoethanolamine-*N*-[carboxy(polyethylene glycol)] powder, >98%, purchased from Shanghai A.V.T. Pharmaceutical Ltd, China) (100 mg) and the above OA-capped MNCs (15 mg, iron content) were mixed together and dissolved in 10 ml chloroform in a 25 ml round-bottom flask, and then, 5 ml deionized water was added gradually to the mixture. After the chloroform was completely vaporized by slow evaporation (65 °C, 20 min), the obtained MNCs@PEG became water soluble.

In the MNCs@RGD synthesis, we firstly activated the –COOH groups on the surface of the above MNCs@PEG. Toelaborate, 1-ethyl-3-(dimethylaminopropyl)carbodiimide hydrochloride (EDC, 100 mg) and *N*-hydroxysuccinimide (NHS, 90 mg) were added to 20 ml 2-(*N*-morpholino)ethanesulfonic acid buffer (MES, 0.02 mol l^{-1}, pH 5–5.5) containing MNCs@PEG (15 mg, iron content). The mixture was then stirred and incubated for 20 min at room temperature. After ultracentrifugation and washing twice with deionized water, the active intermediates dispersed in borate buffer (0.02 mol l^{-1}, pH 8.0), and then 10 mg cyclic RGD peptide was slowly added. The reaction was allowed to stir continuously at room temperature for 24 h. The MNCs@RGD were obtained by centrifugation and washed 3 times with deionized water. The excess empty lipid micelles were removed from the depositing MNCs by ultracentrifugation (100 000*g*). Finally, the purified MNCs@RGD were centrifuged at 3000*g* and the large aggregates were then discarded.

In order to load the ICG as a tricarbocyanine dye into as-synthesized MNCs@PEG and MNCs@RGD respectively, the ICG water solution (1 ml) at a concentration of 1 mg ml^{-1} was mixed with the MNCs (15 mg, iron content). The mixture was then placed on a shaker and incubated overnight at room temperature. The unloaded ICG molecules were gradually removed by repeated ultracentrifugation at 100 000*g*.

Mn–Zn ferrite MNC characterization

The morphology of multi-modal Mn–Zn ferrite MNCs@PEG and MNCs@RGD was observed by using a transmission electron microscope (TEM, Tokyo JEOL, Japan), in which the MNCs dispersed on amorphous carbon-coated copper grids for TEM analysis. The hydrodynamic diameters and surface charges of these MNCs were measured with a particle size/potential analyzer (Malvern Zetasizer, UK). The iron concen-

tration of MNCs were measured with a classical C–A (absorbance *versus* iron concentration) calibration curve, which was established with a 1,10-phenanthroline spectrophotometric method on a UV-visible spectrophotometer (UV-3600, Shimadzu, Japan).[16,17] The magnetism of MNCs was obtained by a vibrating sample magnetometer (VSM, Lakeshore 7407, USA).

T_2-Weighted MR imaging *in vitro*

The MRI experiment of Mn–Zn ferrite MNCs@PEG and MNCs@RGD *in vitro* was carried out on a clinical 1.5 T MR scanner (Avanto, Siemens, Germany). The T_2 relaxation times were determined by the multi-echo spin-echo sequence [16 echoes; repetition time (TR) = 2500 ms; echo time (TE) = 22–352 ms]. For each sample, T_2-weighted MR images of different Fe concentration samples (2.23, 2.79, 4.46, 5.58, 8.93, 11.16, 17.86, 22.32 × 10^{-3} mM) were observed. The T_2 values were obtained by calculating the signal intensity in the 0.3 cm^2 region of interest on each image. The r_2 as a standardized contrast enhancement indicator was calculated as the gradient of the plot of R_2 ($R_2 = 1/T_2$) *versus* the molarity of magnetic atoms.

Heat induction measurements *in vitro*

Measurement of heat generation of Mn–Zn ferrite MNCs@PEG and MNCs@RGD *in vitro* was carried out using a moderate radio frequency heating machine (Shuangping SPG-06-II, China). The samples at a concentration of 2 mg Fe per ml were placed inside a copper coil under an ACMF (390 kHz, 2.58 kA m^{-1}). The SAR value of MNCs is defined as the amount of heat generated per unit gram of magnetic material per unit time, and highly determines the heating ability of MNCs when the ACMF is applied. The SAR value is calculated with the following formula: $SAR = C_w(dT/dt)(m_s/m_m)$, where C_w is the specific heat capacity of the suspension (specific heat capacity of water is 4.18 kJ kg^{-1} K^{-1}); dT/dt is the initial slope of temperature *versus* time graph; m_s is the mass of the suspension, and m_m is the mass of the magnetic material in the suspension.[16,17]

Cellular uptake and specific binding

The RAW264.7 macrophages, HUVECs and 4T1 cells were respectively used to measure the cellular uptake and specific cellular binding of Mn–Zn ferrite MNCs. Comparatively, the RAW264.7 macrophages were incubated with the MNCs@PEG, MNCs@RGD and MNCs@DMSA at a concentration of 60 μg Fe per ml in each well of a 24-well plate with 10^5 cells per well (n = 4 per group). After 12 h, the cells were washed with phosphate buffered saline (PBS) 3 times, fixed with 4% paraformaldehyde and stained with nuclear fast red for 30 min. To stain the intracellular iron, a Prussian blue solution mixed with 2% hydrochloric acid aqueous solution and 2% potassium ferrocyanidetrihydrate was incubated with the fixed cells for 30 min. These cells were finally placed on a microscope for further cellular uptake observation. For MTT assay, the RAW 264.7 macrophages, HUVEC cells and 4T1 cancerous cells were incubated in 96-well plates at a density of 10^5 per well and grown overnight (n = 4 per group), and then co-incubated with a series of concentrations (0–160 μg Fe per ml) of MNCs at 37 °C for 48 h. The experimental process was in accord with previous work.[17]

Animal protocol

Female BALB/c mice aged 4–6 weeks (20–25 g in weight, n = 3–5 per group) were purchased from the Model Animal Research Center of Southeast University. All the animal care and experimental procedures were performed according to the Animal Experimentation Guidelines with the approval of the Animal Care Committee of Southeast University. To establish an experimental model of mice breast tumor, the inoculation with 4T1 cells (5 × 10^6) was accomplished by subcutaneous injection into the right legs of mice. The tumors were then used for imaging diagnostics and therapy after the implantation at the 7th day when they grew to 50–70 mm^3.

In vivo MRI experiments

The *in vivo* MRI experiments of Mn–Zn ferrite MNCs were performed with the use of a 38 mm circular surface coil and a mouse cradle on a 7.0 T Micro-MRI (PharmaScan, Brukers, Germany). Mice were initially anesthetized with a 4% isoflurane/air gas mixture delivered through a nose cone and maintained a body temperature of 37 °C. MR imaging of mice was performed prior to the tail vein injection of the MNCs (30 μg Fe per g body weight) and at appropriate time points post injection, which was taken with T_2 and T_2*-weighted flash sequences. The parameters were as follows: TR/TE = 408 ms/3.5 ms, flip angle = 30°, FOV = 35 mm × 35 mm, slice thickness = 1 mm, matrix = 256 × 256. The total MR imaging time for each time point was less than 40 min. In addition, the MRI quantification measurements were made using ImageJ software, which was based on the overall signal-to-noise ratio of the MR images. The circular areas were selected manually by drawing regions on the T_2*-weighted MR images *in vivo*, and the relative signal intensity (RSI) defined as the ratio of the average signal intensity (SI) in the tumor area (SI_{tumor}) to the SI in the adjacent normal muscle area (SI_{muscle}) of each image was obtained before and after injection of MNCs at different time points.

Fluorescence imaging *in vivo*

The Mn–Zn ferrite MNCs/ICG and free ICG molecules were intravenously injected into tumor bearing mice through the tail vein and the fluorescence images were taken by the total internal reflection fluorescence microscopy (Maestro 2.10.0, CRI, USA) model after injection at different time points. A filter set (E_x = 745 nm, E_m = 810 nm) was used for the measurement of ICG. During the imaging process, the mice were kept on the imaging stage under anesthetized conditions with a 4% isoflurane/air gas mixture delivered through a nose cone and maintained a body temperature of 37 °C. Scans were performed at 20 min, 2 h, 4 h, 12 h and 24 h after the intravenous injection of MNCs. After the imaging process, the tumor bearing mice were sacrificed and the main organs (heart, liver, spleen, lung and kidney) were taken out for determining the distribution of MNCs *in vivo*. To compare the targeting ability

of MNCs@PEG and MNCs@RGD groups, TBR values between the tumor and adjacent normal muscle at different time points were calculated by using regions of interest (ROI) functions of the Maestro 2.10.0 software. Circular ROIs were selected manually by drawing regions on the *in vivo* optical images. The TBR was calculated using the following formula: $TBR = SI_T/SI_M$, where SI_T is the average signal of the tumor and SI_M is the average signal of the contralateral thigh muscle. This procedure was carried out as described by Alencar and Tang *et al.*[34,35]

TMH experiments *in vivo*

All MNC-induced TMH experiments *in vivo* were carried out safely using a moderate radio frequency heating machine (390 kHz, 2.58 kA m^{-1}). The mice were placed in the induction coil using a specially designed Teflon supporter, in which the tumors were located exactly in the region of the ACMF possessing the highest field density. The tumor surface and the surrounding skin temperature measurements were monitored using an infrared-thermograph (Fulke, Ti32, USA). The effective antitumor effects were determined on mice with tumors of diameter 50–80 mm^3. The tumor volumes were calculated from the formula: $V = AB^2\pi/6$, where A is the longer and B is the shorter lateral diameter of the tumor. Relative tumor volume ratio (RTV) values were calculated as $(V - V_0)/V_0$ (V_0 is the tumor volume when the treatment was initiated).[17]

Tumor tissue iron content measurement

Quantitative kinetic studies of MNC tumor uptake levels were carried out. To completely release iron, the tumor tissues were firstly digested with a strong acid mixture of 1 M H_2SO_4 and 1 M HNO_3 and heated to 60 °C. After the tissues were mostly dissolved (3–4 days), 6 M HCl was then added at a 3 : 1 (HCl/HNO_3) ratio. The MNC amounts in the tumor were then given in micrograms of Fe per gram of *ex vivo* tumor tissue after the injection through the mice tail vein. Similar to Fe concentration measurement of MNCs *in vitro*, the tumor tissue iron concentration was also measured with a C–A calibration curve, which was established with the 1,10-phenanthroline spectrophotometric method on a UV-visible spectrophotometer.[16,17]

Histochemical, immunohistochemistry and biological TEM analysis *in vivo*

For histochemical analysis, the tumor tissues from mice were excised and fixed in 10% neutral buffered formalin for 2 weeks, and then the tissues were processed routinely into paraffin, sectioned at a thickness of 3–5 mm, stained successively by Prussian blue for MNCs and nuclear fast red for the cell nucleus, and finally examined by optical microscopy. In addition, the other sections of tumor tissues were used for TUNEL staining, which was performed with an *in situ* apoptotic cell detection kit according to the manufacturer's directions (Promega).[17] The apoptotic cells were identified by positive TUNEL staining (brown color) under an optical microscope, and the four randomly microscopic fields in each group were used to study the percentages of apoptotic cells.

To examine the TMH effects on tumor microvessels, an immunohistochemical analysis was further performed. Here the tumor sections were firstly probed with a monoclonal rat anti-mouse CD31 (vascular endothelial cell marker) antibody (1 : 400) at 4 °C overnight, followed by incubation with a biotinylated polyclonal goat anti-rat antibody (1 : 200), in a humidified chamber for 1 h, and were then immersed in 0.3% H_2O_2 in absolute methanol for 15 min to block endogenous peroxidase. Finally, the sections were counterstained with hematoxylin and mounted with glass coverslips, and were visualized in an optical microscope.

For biological TEM analysis, tumor tissues were fixed overnight with 2.5% glutaraldehyde, and were further cut into small pieces of ~1 mm^3. In succession, the tissue specimens were stained overnight using 1% uranyl acetate in the dark, and were dehydrated using increasing concentrations (from 25% to 100%) of ethanol alcohol. Lastly, the fully dehydrated tissues were embedded in resin, which was then cured in an oven at a temperature of 60 °C (2 days) for TEM observation.

Conclusions

In summary, we successfully synthesized monodisperse Mn–Zn ferrite MNCs@PEG and MNCs@RGD with an ideal core–shell structure. In terms of their excellent biocompatibility and high magnetic heat induction ability, they were here used for effective TMH in cancer therapy. The first challenge in our work was designing an effective MNC-mediated theranostics strategy by a combination of simultaneous tumor multi-modal images and TMH therapy. It not only provided the real-time monitoring of the MNC localization and accumulation on tumor regions, evaluated the tumor morphology and volume when exposed to an ACMF by means of fluorescence imaging- or MRI-guided tumor diagnosis, but also duly evaluated and adjusted the optimal strategies based on tumor surface infrared-thermal imaging (*e.g.* adequate intravenous injection dose and sufficient hyperthermia duration). Furthermore, the second challenge was that we systematically compared the MNCs@PEG- and MNCs@RGD-based tumor passive and active (vascular) targeting efficiency by intravenous administration, including quantitative tumor uptake, intracellular location and retention time *in vivo*. More importantly, to our knowledge, it was found that the MNCs@RGD-based active target ability was significantly more efficient within a certain period of time, leading to higher *in vivo* MR imaging. The MNCs@RGD simultaneously functionalized with a PEG chain and RGD ligands promoted the synergistic tumor vascular active targeting and the EPR-mediated passive targeting, achieving the heat-induced apoptosis of tumor cells and suppression of tumor-associated angiogenesis *in vivo* in TMH therapy. But its antitumor efficacy was not obviously improved in the TMH treatments compared with MNCs@PEG, due to the lack of effective and markedly increased MNC content in tumor tissue. We

believe that our synthesized active MNCs@RGD as excellent heating agents, further combined with some targeted anti-cancer drugs, will have more promising cancer theranostics applications.

Acknowledgements

This research was supported by the National Important Science Research Program of China (no. 2011CB933503, 2013CB733800), the National Natural Science Foundation of China (no. 81571806), the National High Technology Research and Development Program of China (no. 2013AA032205), the Jiangsu Provincial Special Program of Medical Science (BL2013029), and the Jiangsu Provincial Technical Innovation Fund for Scientific and Technological Enterprises (no. SBC201310643).

Notes and references

1 C. Yang, J. J. Wu and Y. L. Hou, *Chem. Commun.*, 2011, **47**, 5130–5141.
2 J. Yu, X. Chu and Y. L. Hou, *Chem. Commun.*, 2014, **50**, 11614–11630.
3 J. Yu, C. Yang, J. D. S. Li, Y. C. Ding, L. Zhang, M. Z. Yousaf, *et al.*, *Adv. Mater.*, 2014, **26**, 4114–4120.
4 J. Yu, Y. M. Ju, L. Y. Zhao, X. Chu, W. L. Yang, Y. L. Tian, *et al.*, *ACS Nano*, 2016, **10**, 159–169.
5 D. Yoo, J. H. Lee, T. H. Shin and J. Cheon, *Acc. Chem. Res.*, 2011, **44**, 863–874.
6 I. Hilger and W. A. Kaiser, *Nanomedicine*, 2012, **7**, 1443–1459.
7 D. K. Chatterjee, P. Diagaradjane and S. Krishnan, *Ther. Delivery*, 2011, **2**, 1001–1014.
8 R. Stone, T. Willi, Y. Rosen, O. T. Mefford and F. Alexis, *Ther. Delivery*, 2011, **2**, 815–838.
9 H. S. Huang and J. F. Hainfeld, *Int. J. Nanomed.*, 2013, **8**, 2521–2532.
10 N. Tran and T. J. Webster, *J. Mater. Chem.*, 2010, **20**, 8760–8767.
11 J. H. Lee, J. T. Jang, J. S. Choi, S. H. Moon, S. H. Noh, J. W. Kim, *et al.*, *Nat. Nanotechnol.*, 2011, **6**, 418–422.
12 S. Balivada, R. S. Rachakatla, H. W. Wang, T. N. Samarakoon, R. K. Dani, M. Pyle, *et al.*, *BMC Cancer*, 2010, **10**, 119.
13 K. Hayashi, M. Nakamura, W. Sakamoto, T. Yogo, H. Miki, S. Ozaki, *et al.*, *Theranostics*, 2013, **3**, 366–376.
14 J. Kolosnjaj-Tabi, R. D. Corato, L. Lartigue, I. Marangon, P. Guardia, A. K. A. Silva, *et al.*, *ACS Nano*, 2014, **8**, 4268–4283.
15 J. T. Jang, H. Nah, J. H. Lee, S. H. Moon, M. G. Kim and J. Cheon, *Angew. Chem., Int. Ed.*, 2009, **48**, 1234–1238.
16 J. Xie, C. Z. Yan, Y. Zhang and N. Gu, *Chem. Mater.*, 2013, **25**, 3702–3709.
17 J. Xie, Y. Zhang, C. Y. Yan, L. N. Song, S. Wen, F. C. Zang, *et al.*, *Biomaterials*, 2014, **35**, 9126–9136.
18 N. Bertrand, J. Wu, X. Y. Xu, N. Kamaly and O. C. Farokhzad, *Adv. Drug Delivery Rev.*, 2014, **66**, 2–25.
19 F. Danhier, B. Ucakar, N. Magotteauxa, M. E. Brewster and V. Préat, *Int. J. Pharm.*, 2010, **392**, 20–28.
20 F. Ungaro, C. Conte, L. Ostacolo, G. Maglio, A. Barbieri, C. Arra, *et al.*, *J. Nanomed. Nanotechnol.*, 2012, **8**, 637–646.
21 M. Kumagai, T. K. Sarma, H. Cabral, S. Kaida, M. Sekino, N. Herlambang, *et al.*, *Macromol. Rapid Commun.*, 2010, **31**, 1521–1528.
22 S. Tong, S. J. Hou, Z. L. Zheng, J. Zhou and G. Bao, *Nano Lett.*, 2010, **10**, 4607–4613.
23 D. F. Liu, W. Wu, J. J. Ling, S. Wen, N. Gu and X. Z. Zhang, *Adv. Funct. Mater.*, 2011, **21**, 1498–1504.
24 N. Lee, Y. Choi, Y. Lee, M. Park, W. K. Moon, S. H. Choi, *et al.*, *Nano Lett.*, 2012, **12**, 3127–3131.
25 S. Kunjachan, R. Pola, F. Gremse, B. Theek, J. Ehling, D. Moeckel, *et al.*, *Nano Lett.*, 2014, **14**, 972–981.
26 J. D. Byrne, T. Betancourt and L. Brannon-Peppas, *Adv. Drug Delivery Rev.*, 2008, **60**, 1615–1626.
27 F. Danhier, O. Feron and V. Préat, *J. Controlled Release*, 2010, **148**, 135–146.
28 C. F. Zhang, M. Jugold, E. C. Woenne, T. Lammers, B. Morgenstern, M. M. Mueller, *et al.*, *Cancer Res.*, 2007, **67**, 1555–1562.
29 P. P. Lv, Y. F. Ma, R. Yu, H. Yue, D. Z. Ni, W. Wei, *et al.*, *Mol. Pharm.*, 2012, **9**, 1736–1747.
30 P. C. Brooks, A. M. P. Montgomery, M. Rosenfeld, R. A. Reisefeld, T. H. Hu, G. Klier, *et al.*, *Cell*, 1994, **79**, 1157–1164.
31 R. Haubner, D. C. Dirk-Finsinger and H. Kessler, *Angew. Chem., Int. Ed. Engl.*, 1997, **36**, 1374–1389.
32 P. A. Burke and S. J. DeNardo, *Crit. Rev. Oncol. Hematol.*, 2001, **39**, 155–171.
33 R. L. Qiao, W. H. Yan, H. Lum and A. B. Malik, *Am. J. Physiol.: Cell Physiol.*, 1995, **269**, C110–C117.
34 H. Alencar, M. A. Funovics, J. Figueiredo, H. Sawaya, R. Weissleder and U. Mahmood, *Radiology*, 2007, **244**, 232–238.
35 Q. S. Tang, Y. L. An, D. F. Liu, P. D. Liu and D. S. Zhang, *PLoS One*, 2014, **9**, e106483.
36 Y. Nishimura, Y. Shibamoto, S. Jo, K. Akuta, M. Hiraoka, M. Takahashi, *et al.*, *Cancer Res.*, 1988, **48**, 7226–7230.
37 C. Roca, L. Primo, D. Valdembri, A. Cividalli, P. Declerck, P. Carmeliet, *et al.*, *Cancer Res.*, 2003, **63**, 1500–1507.

